Applied Materials Today 16 (2019) 482–492

Contents lists available at ScienceDirect

Applied Materials Today

journal homepage: www.elsevier.com/locate/apmt

A versatile PDMS submicrobead/graphene oxide nanocomposite ink for the direct ink writing of wearable micron-scale tactile sensors

Ge Shi[a,1], Sean E. Lowe[a,1], Adrian J.T. Teo[b], Toan K. Dinh[b], Say Hwa Tan[b], Jiadong Qin[a], Yubai Zhang[a], Yu Lin Zhong[a,*], Huijun Zhao[a,*]

[a] Centre for Clean Environment and Energy, School of Environment and Science, Gold Coast Campus, Griffith University, Gold Coast, Queensland 4222, Australia
[b] Queensland Micro- and Nanotechnology Centre, Griffith University, 170 Kessels Road, Brisbane, Queensland 4111, Australia

ARTICLE INFO

Article history:
Received 8 May 2019
Received in revised form 25 June 2019
Accepted 29 June 2019

Keywords:
PDMS
Graphene oxide
Nanocomposite
Direct ink writing
Tactile sensor

ABSTRACT

Although direct ink writing (DIW) is a versatile 3D printing technique, progress in DIW has been constrained by the stringent rheological requirements for printable conductive nanocomposites, particularly at smaller length scales. In this work, we overcome these challenges using an aqueous nanocomposite ink with polydimethylsiloxane (PDMS) submicrobeads and an electrochemically derived graphene oxide (EGO) nanofiller. This nanocomposite ink possesses a thixotropic, self-supporting viscoelasticity. It can be easily extruded through very small nozzle openings (as small as 50 μm) allowing for the highest resolution PDMS DIW reported to date. With a mild thermal annealing, the DIW-printed device exhibits low resistivity (1660 Ω·cm) at a low percolation threshold of EGO (0.83 vol.%) owing to the unique nanocomposite structure of graphene-wrapped elastomeric beads. The nanocomposite ink was used to print wearable, macro-scale strain sensing patches, as well as remarkably small, micron-scale pressure sensors. The large-scale strain sensors have excellent performance over a large working range (up to 40% strain), with high gauge factor (20.3) and fast responsivity (83 ms), while the micron-scale pressure sensors demonstrated high pressure sensitivity (0.31 kPa^{-1}) and operating range (0.248–500 kPa). Ultrahigh resolution, multi-material layer-by-layer deposition allows the engineering of microscale features into the devices, features which can be used to tune the piezoresistive mechanism and degree of piezoresistivity.

1. Introduction

With the rise of mobile devices and technology, there is a growing demand for smart, wearable devices for various applications, including wearable energy generation and storage [1,2], smart medical patches [3], and human–computer interaction devices [4]. Tactile sensing [5] is a crucial component for wearable devices designed to measure or respond to human movement. Such devices typically need to measure pressures between 1 and 100 kPa [6–8]. Piezoresistive type sensors are often deployed in this case due to their high sensitivity and easy fabrication [9]. Polydimethylsiloxane (PDMS) is often used to encapsulate such piezoresistive-type sensors. PDMS is widely used for flexible electronics, microfluidics and medical devices due to its biocompatibility, optical transparency, low autofluorescence, excellent moldability and high oxygen permeability [10].

3D printing has recently emerged as a solution for creating PDMS-based structures [5,11–18]. Direct ink writing (DIW), a type of 3D printing, can construct 3D microstructures via layer-by-layer deposition of polymer composite ink of typically high viscosity [19,20]. DIW can construct 3D devices from multiple nanocomposite ink components and allows for shear-induced microstructuring of nanofillers during ink extrusion [21]. The control of the materials composition and their interactions has to be well-optimized for the desired device properties [22].

DIW of conductive PDMS elements is challenging on at least two fronts. Firstly, the viscosity of PDMS must be tailored for 3D printing. Commercially available PDMS precursors have a watery consistency and will not hold their shape after DIW extrusion. Previous efforts have used salts [12], nanosilica additives [13], or shear thinning silicon rubber [23] to thicken the PDMS ink. Ideally, the ink should flow easily but possess self-supporting viscoelasticity after extrusion (i.e., thixotropic behavior) [19]. Particularly challenging is the miniaturization of DIW PDMS nanofillers; as printing nozzles become smaller, extrusion of viscous fluids becomes exceedingly

* Corresponding authors.
E-mail addresses: y.zhong@griffith.edu.au (Y.L. Zhong), h.zhao@griffith.edu.au (H. Zhao).
[1] Both these authors contributed equally to this work.

https://doi.org/10.1016/j.apmt.2019.06.016
2352-9407/

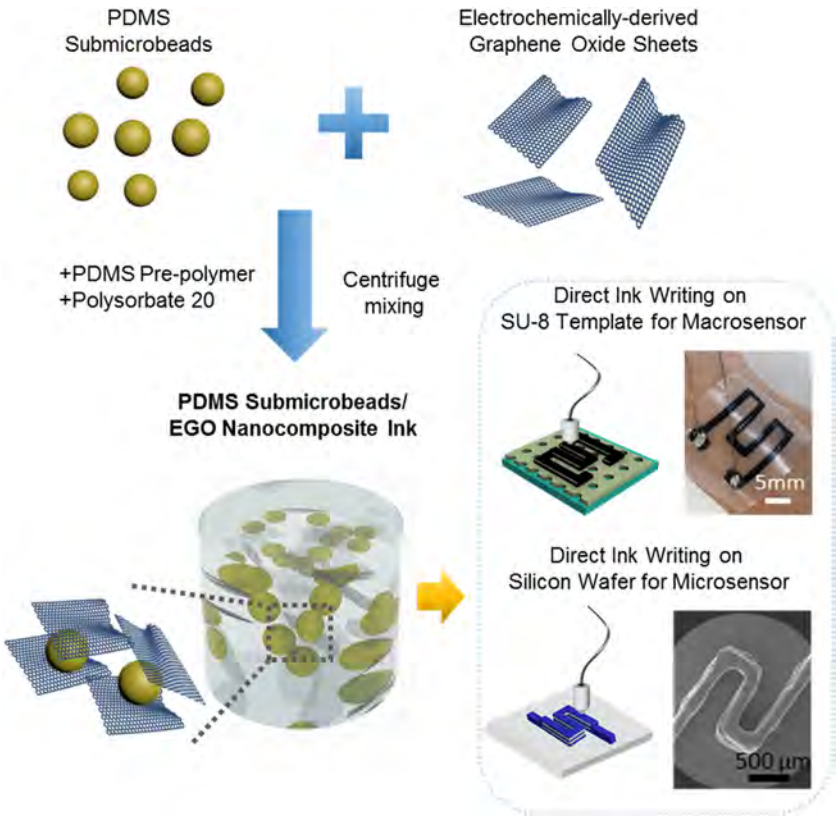

Fig. 1. Overview of the fabrication of PDMS submicrobead/EGO nanocomposite ink and 3D DIW of wearable macrosensor and microsensor.

difficult. Overcoming this challenge requires novel approaches in the design and formulation of the nanocomposite inks [24]. Herein, we find that PDMS can itself be pre-cured into submicrobeads that, together with a surfactant and graphene nanofiller, have the effect of markedly improving the viscoelastic properties of the ink for DIW.

A second challenge associated with PDMS is incorporation of conductive materials into PDMS matrices. Typically, PDMS is hydrophobic with limited compatibility with water and most solvents, limiting the dispersibility of hydrophillic conductive materials into PDMS [25]. A strategy to improve the water compatibility, and hence processability, of PDMS is to synthesize water soluble PDMS or surfactant-wrapped PDMS emulsions [26]. This strategy provides a controlled way to introduce the elastic component to inks via water-dispersible PDMS beads [27,28]. In terms of the conductive component of inks, while silver is often used in PDMS composites [5,13,16], for larger scale/commercial implementation, lower cost nanofillers would ideally be used. Carbon-based nanofillers such as graphene oxide are one alternative.

In this work, a new formulation strategy was developed which allows for the introduction of low cost, electrochemically derived graphene oxide (EGO) [29] and PDMS submicrobeads into an aqueous nanocomposite ink, ink which was subsequently used for DIW 3D printing (Fig. 1). The ink's finely tuned rheology allows it to be extruded from nozzles as small as 50 μm, allowing us to print conductive nanocomposite structures with unparalleled resolution. A strain sensing wearable patch which is highly sensitive (capable of detecting human pulse) and robust (>1000 cycle stability) was developed, the performance being comparable to or exceeding the best reported low cost carbon-nanofiller-based devices. Furthermore, this design is miniaturized to create a microscale pressure sensor. The device is produced using layer-by-layer deposition, with each layer being ~100 μm thick. By engineering micro-gaps between the layers, we can drastically modulate the device's piezoresistivity to achieve excellent sensitivity (detecting forces as low as 248 Pa) but good operating range (up to 500 kPa). This 3D DIW approach has broad applications for device miniaturization, enabling space efficient, yet flexible, tactile sensing components.

2. Materials and methods

2.1. Materials

Graphite flakes (Sigma-Aldrich 332461) were the starting material for the synthesis of electrochemically derived graphene oxide (EGO). Polydimethylsiloxane (Sylgard 184, Dow Corning) was purchased from Sigma-Aldrich and used to fabricate the nanocomposite ink. Polyvinyl alcohol (PVA) (Mowiol 18-88) with molecular weight ~130,000 and dichloromethane were purchased from Sigma-Aldrich. Polysorbate 20 (Sigma-Aldrich item 44112) was used as the emulsifier to form PDMS submicrobead dispersions in aqueous solution. For the EGO synthesis, the working electrode plate consisted of niobium coated with CVD-grown polycrystalline boron-doped diamond (BDD) (Diaccon GmBH, Fürth, Germany). The cell separator consisted of glass microfiber filters (pore size 0.7 μm, Whatman brand from GE Healthcare, Chicago, Cat. No. 1825-047). The counter electrode was made from 0.25-mm diameter platinum wire (Item 850-988-64, Goodfellow, Cambridge, UK). THF and 98% sulfuric acid were purchased from ChemSupply (Gillman, SA, Australia).

2.2. Synthesis of PDMS submicrobeads

PDMS submicrobeads were synthesized in an emulsion-based process. 8 g of PDMS pre-polymer with the ratio of base to curing

agent of 10:1 was dissolved in 4 g of DCM and then mixed with 40 g of 5.83 wt.% PVA aqueous solution. The optimal concentration of PVA was found to be 5.83 wt.% due to the high molecular weight of PVA (~130,000) which made it difficult to obtain PVA solution with higher concentration. Therefore, DCM was employed in the emulsion, which evaporated after drying, thus affording a reduced PDMS submicrobead size.

The solution was then emulsified with a Silverson electronic rotor-stator mixer (L5M-A) for 40 min at 10,000 rpm. The PDMS emulsion was then placed on a hot plate and magnetically stirred (200 rpm) in a fume hood at 50 °C for 8 h to evaporate DCM and cure PDMS submicrobeads.

After curing, 20 g of DI water was added to the PDMS submicrobeads. This solution was then centrifuged for 40 min at 14,000 rpm (Dynamica, Velocity 18R centrifuge). After decanting the supernatant of the PVA aqueous solution away, PDMS submicrobeads were left as sediment. 60 g of DI water was added to the PDMS submicrobead sediment, and the mixture was ultrasonicated for 2 min to disperse the submicrobeads. The suspension was centrifuged again at 14,000 rpm for 15 min, and the PVA aqueous solution was decanted away. The centrifuge-ultrasonication-wash process was repeated 3 times to remove PVA and form a sediment of PDMS submicrobeads. For the insulating layer in the microscale pressure sensor, the sediment (500 mg/mL) was put into a 10 mL plastic syringe as ink for direct writing. At this high concentration, the suspension displays a gel-like behavior and can be 3D printed.

2.3. Production of graphene oxide in a packed-bed electrochemical reactors

EGO was synthesized in a custom-made 3D printed packed bed reactor as reported previously [29], except that the starting graphite was pre-sieved to remove particles less than 300 μm in diameter. To synthesize the EGO, in brief, 3.95 g of sieved graphite flakes were loosely packed without binder into a rectangular compartment forming an electrochemical cell. At the bottom of the compartment, the graphite contacted a BDD working electrode that formed the base of the cell. The surface area of the graphite bed touching the working electrode was 12.15 cm^2. Glass fiber membranes were placed atop the graphite bed, and the graphite and membrane were pressed against the diamond electrode by a weighted plastic press. A coiled platinum wire counter electrode was placed within the cell above the graphite bed. The graphite was then oxidized with a constant current of 15.59 mA/cm^2 in an 11.6 M sulfuric acid electrolyte. The reaction was allowed to run until the whole cell voltage reached 12 V (approximately 28 h). The product was then removed from the reactor and thoroughly washed with Milli-Q water and resuspended to a concentration of ~6.8 mg/mL.

After obtaining the EGO suspension, ~5 g of 30 wt.% ammonia solution was added into a ~100 g EGO suspension to increase the pH to 12. The basic EGO suspension was subjected to 2 h of ultrasonication via an ultrasonic homogenizer (JY92-IIDN, Ningbo Scentz Biotechnology Co., Ltd, China). The exfoliated EGO suspension was centrifuged at 4400 rpm for 20 min to produce an EGO slurry in the sediment. The EGO slurry was dispersed in 100 g DI water and centrifuged again at 4400 rpm for 20 min to remove ammonia, resulting in EGO sediment with concentration of ~80 mg/ml.

2.4. Formulation of PDMS submicrobead/EGO nanocomposite ink

The nanocomposite ink for DIW was prepared as follows. First, 7.5 ml of the as-prepared, ~80 mg/ml EGO aqueous suspension was mixed with 3.2 g of PDMS submicrobead sediment (~500 mg/ml) and 10 mg of Polysorbate 20 with a vortex mixer. Second, 0.6 g of PDMS pre-polymer was added to the aqueous solution. Next, the resulting composite was mixed using a planetary centrifugal mixer (DB-988, Foshan COXO Medical Instrument Co., Ltd, China) at 1500 rpm for 10 min to remove bubbles and obtain a homogeneous, gel-like mixture.

2.5. Fabrication of SU-8 template

A 4-inch silicon wafer was first baked at 150 °C for 10 min on a hotplate for dehydration. Bisphenol A Novolac epoxy (SU-8 3010, MicroChem Corp., USA) was spin-coated onto the wafer (2,000 rpm, 30 s), followed by soft baking for 5 min at 150 °C and relaxation for 5 min. The Si wafer was then mounted onto the chamber of a photolithographic machine. The wafer was exposed to UV (λ = 365 nm, dose = 150 mJ cm^{-2}) for 150 s with a photomask having a microhole array, followed by 5 min of relaxation. After the UV exposure, the wafer was further baked at 100 °C for 3 min and relaxed for 5 min. Subsequently, the UV-exposed SU-8 layer was developed using an SU-8 developer (Microchem Corp, USA) for 5 min, followed by rinsing with isopropyl alcohol and blow-drying with nitrogen. The SU-8 film was hardbaked again at 150 °C for 10 min to produce an SU-8 template. Finally, the substrate was rinsed with deionized water and blow-dried with nitrogen.

2.6. DIW of wearable macro-strain sensor and micro-pressure sensors

The PDMS submicrobead/EGO nanocomposite ink was printed using an nScrypt 3Dn-300 printer equipped with two SmartPumps and ceramic nozzles with tip diameters of 50, 100 or 200 μm. The wearable, macro-strain sensor was printed with the 200 μm nozzle, and the small micro-sensor was printed with the 100 μm nozzle. The open travel distance of the valve rod was 0.6 mm, and the extrusion air pressure was adjusted to ~4.5 psi for the large-scale sensor and ~8.0 psi for the smaller/micro-pressure sensor. For fabrication of the macro-strain sensor, the ink was extruded on an SU-8 template held in place by the 3D printer's vacuum stage. For fabrication of the 3D microsensor, inks were extruded onto a silicon wafer and allowed to warm to 50 °C on the 3D printer's hotplate.

After DIW, the SU-8 template with printed sensor component was placed in an oven in air at 50 °C for 2 h to evaporate the water and cure the liquid PDMS. Then, the sensor was place in an oven at 200 °C in air for 1 h to thermally anneal the EGO and increase its conductivity. Next, silver paste and silver conductive connection wire were bonded onto the sensor. Lastly, 5 g of PDMS pre-polymer was drop cast onto the SU-8 template and cured with the sensor component at 50 °C for 1 h.

2.7. Fabrication of control PDMS polymer/EGO nanocomposite

PDMS polymer/EGO nanocomposites (without submicrobeads) were prepared by a solution compounding method at room temperature. An ultrasonicated EGO suspension (described above) of roughly 6.8 mg/mL was centrifuged at 4400 rpm, and the sediment (80 mg/ml) was freeze dried to produce an EGO aerogel. The aerogel was reductively deoxygenated by thermally annealing at 200 °C in air for 1 h. Then, 400 mg of the annealed EGO aerogel was ultrasonicated in 90 g THF for 20 min to prepare an annealed EGO/THF suspension. Subsequently, this suspension was mixed with liquid PDMS pre-polymer. Different ratios of the EGO/THF suspension and PDMS pre-polymer were mixed to achieve EGO mass loadings from ~0.4 to 4.0 wt.%. After high shear mixing for 10 min at 5000 rpm, the suspension was poured into a mold. The mixture was heated at 60 °C for 2 h in air to evaporate the THF and cure the PDMS.

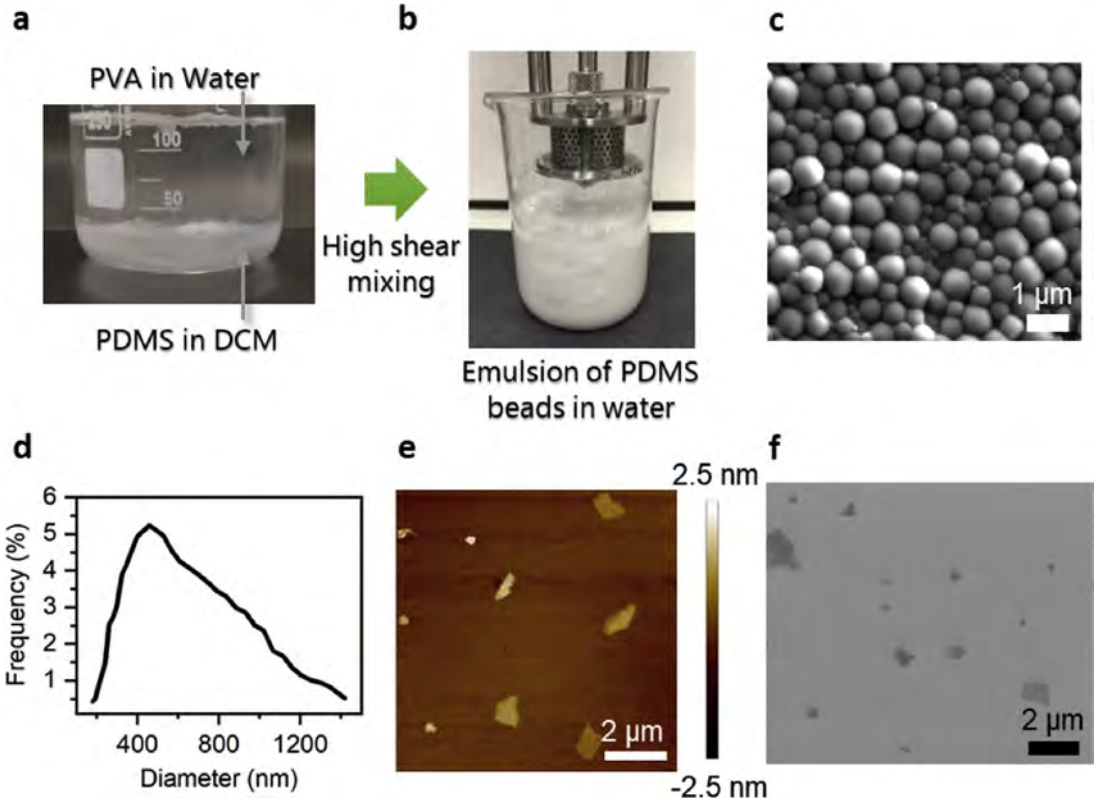

Fig. 2. Ink components preparation and characterization. (a–b) Emulsion synthesis of PDMS submicrobeads. The PDMS pre-polymer in DCM and the surfactant PVA in the supernatant before mixing (a). After high shear mixing at 10,000 rpm for 40 min, the smooth dispersion shown in (b) evolves. (c) SEM micrograph of packed PDMS submicrobeads after curing/drying. (d) Size distribution of the PDMS submicrobeads. (e) AFM and (f) SEM micrographs of EGO sheets after ultrasonication.

2.8. Materials characterization

Scanning electron microscope (SEM) micrographs were obtained using a Joel JSM-7500FA microscope (Jeol Ltd., Japan) with an accelerating voltage of 15 kV. Atomic force microscopy (AFM) images were collected with a Bruker Dimension Icon AFM using peak force tapping mode. Thermogravimetric analysis (TGA) of EGO, PDMS submicrobead/EGO nanocomposite samples was performed on a Netzsch STA 449F3 analyzer (NETZSCH group, Germany) in a 20% oxygen/80% argon environment. XPS data was acquired using photon energy of 1486 eV from the Soft X-ray Spectroscopy beamline at the Australian Synchrotron with a SPECS Phoibos 150 hemispheric analyzer. Binding energies of all XPS spectra were calibrated using a clean gold foil in electrical contact with the samples.

An Anto Paar MCR 702 MultiDrive rheometer was used to analyze the rheological properties of nanocomposite inks under ambient conditions. A solvent trap was applied to limit evaporation during the measurements.

2.9. Device characterization and testing

The surface morphology and the cross-sectional structure of the strain sensors were characterized with the Joel SEM described above with accelerating voltage of 15.0 kV. A digital source meter (Keithley 2604, Tektronix Inc., Beaverton, OR, USA) was employed to measure the resistance and change of resistance of the strain sensors under different loadings. Tensile strain was applied to the sensor with a programmable Instron 5567 system (Instron, Norwood, MA, USA) and simultaneous resistivity measurements were collected with the source meter under a constant voltage of 1 V. During tensile testing, the top end of the strain sensor and the bottom end (with silver paste contacts) were held by the clamps of the Instron system.

The sensor durability was investigated by applying cyclic loading at a frequency of 4 s per cycle; all sensors were stretched at strain values of 10% and 20%. The response time was recorded as the delay time between the loading start point and resistance change stop point [30]. The resistance change for the response time measurement was recorded while applying 2% tensile strain at a speed of 100 mm s^{-1}. Pressure sensing performance was recorded by placing small pieces of glass weighing 20, 30, 45, 75 or 95 mg and poise weights and metal bars weighing 1, 2, 5, 10, 20 or 40 g onto the sensor and recording the resistivity. As shown in Fig. S15b, to avoiding a short circuit, a thin film of Parafilm was put on the sensor before placing the poise weight or metal bars. The dynamic response of the sensors was measured by taping the microsensors to a gloved finger and holding the sensor against the vibrating rubber head of a vortex mixer set to 300 rpm.

3. Results and discussion

To achieve a thixotropic ink capable of high-resolution DIW, we first improved the viscoelastic properties of PDMS by developing PDMS submicrobeads. These submicrobeads were subsequently integrated with our EGO nanofiller for printing a range of functional tactile sensors.

3.1. Emulsion synthesis of PDMS submicrobeads

PDMS submicrobeads were produced using an oil/water phase emulsion illustrated in Fig. 2a and b. A PDMS pre-polymer (base and curing agent)/dichloromethane (DCM) solution was initially mixed with a PVA aqueous solution, leading to phase separation. After

high shear mixing, the PDMS/DCM solution was emulsified due to the surfactant properties of PVA. During the shearing process, the emulsion was pressed through the narrow gap between the stator and rotor blades [31,32], where the turbulent shear forces created PDMS/DCM droplets of ~1 μm in diameter (Fig. S1a). After evaporation of the DCM at 50 °C for 2 h, the PDMS droplets were cured as submicrobeads and suspended in the solution.

The SEM micrograph and size distribution of these submicrobeads is shown in Fig. 2c and d, respectively. The submicrobeads have a mean diameter of 836 ± 583 nm (mode of 459 nm). The solvent, DCM, plays a key role in reducing the lateral dimension of the submicrobeads. Because it can effectively reduce the viscosity of the PDMS pre-polymer solution [33], it facilitates droplet shearing down to submicrometer size [34]. PDMS pre-polymer has a higher viscosity without the DCM solvent (3.5 Pa s at a shear rate of 10 s^{-1}) [35], compared to its viscosity with DCM (4.1×10^{-4} Pa s) [36]. Without DCM, the average size of PDMS beads was ~3.6 μm (Fig. S1).

3.2. Synthesis and ultrasonic exfoliation of EGO

Electrochemistry has recently been shown to be a promising method for the production of graphene oxide (GO) from natural flake graphite [37,38], capable of overcoming many of the limitations of the chemical GO route [39]. We chose EGO as a practical nanofiller because its synthesis is relatively low-cost and scalable and because it has a notably high conductivity after low-temperature thermal annealing [29]. EGO for the current study was synthesized in our recently reported 3D printed packed bed reactor (Fig. S2) [29]. Here, graphite flakes are anodically oxidized, resulting in graphite oxide that can be readily exfoliated to few-layer graphene oxide.

In this case, the electrochemically produced graphite oxide was exfoliated by ultrasonication for 2 h, reducing the lateral flake dimensions to a size suitable for extrusion through nozzles as small as 50 μm. Typical SEM and AFM micrographs of the EGO are presented in Fig. 2e and Fig. S3. Particle size and thickness analysis

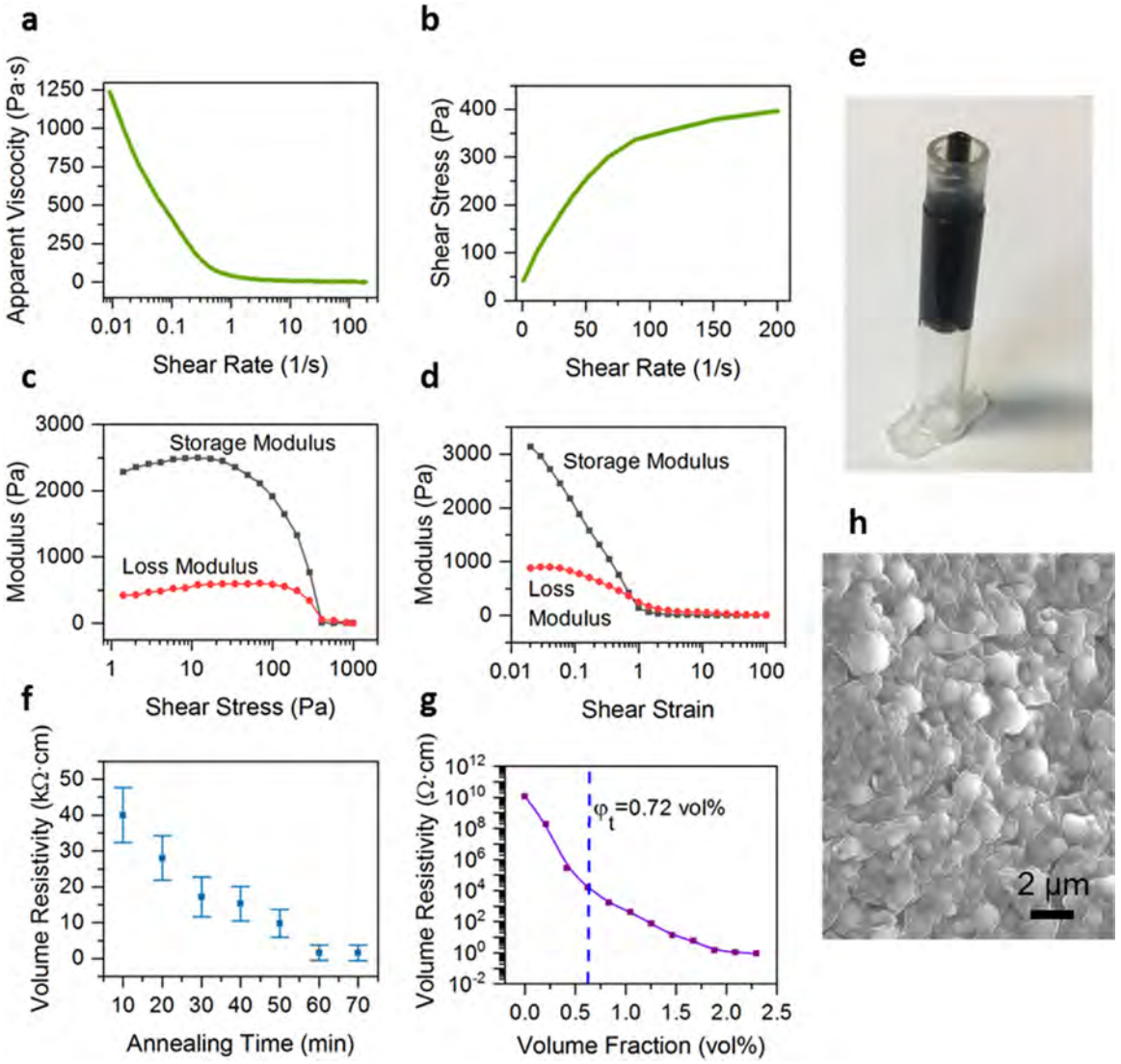

Fig. 3. Ink rheology and thermal annealing. (a) Apparent viscosity as a function of shear rate. (b) Shear stress as a function of shear rate. (c–d) The shear modulus as a function of shear stress (c) and shear strain (d). (e) Photograph of a syringe containing PDMS submicrobead/EGO nanocomposite ink, which does not flow without external pressure. (f) Volume resistivity a function of thermal annealing at 200 °C in air of the composite ink at 0.83 vol.% EGO. (g) Volume resistivity after thermal annealing (200 °C for 1 h) as a function of EGO volume fraction. (h) SEM micrograph of cured ink consisting of EGO-encapsulated PDMS submicrobeads.

indicates that most EGO sheets have average lateral dimensions of 0.77 μm and few layer or single layer thickness (Fig. S3g–h). The XPS C 1s spectrum (Fig. S4a) shows the presence of hydroxyl or epoxide groups (C—OH or C—O—C), and carbonyl (C=O) and carboxyl groups (COOH). The XPS survey spectrum in Fig. S4b suggests a C/O ratio of ~3.67.

3.3. Formulation of printable PDMS submicrobead/EGO nanocomposite ink

The nanocomposite ink was comprised of PDMS submicrobeads (14.2 wt.%), EGO (5.3 wt.%), PDMS pre-polymer (5.3 wt.%), Polysorbate 20 (0.09 wt.%) and water (75.2 wt.%). Suspensions of PDMS submicrobeads and EGO sheets were mixed, and Polysorbate 20 was then added. Polysorbate 20 is a nonionic amphiphilic surfactant containing hydrophilic and hydrophobic moieties [40]. In the mixture, the Polysorbate 20 surfactant can also adsorb to the PDMS submicrobeads and EGO sheets, leading to a stabilization effect [23]. Next, PDMS pre-polymer was incorporated with a centrifugal mixer. PDMS pre-polymer would bind with PDMS submicrobeads/EGO sheets with the assistance of Polysorbate 20. PMDS pre-polymer will wet the surface of PDMS submicrobeads/EGO sheets. This will lead to the agglomeration of PDMS submicrobeads/EGO sheets and create a sample-spanning network due to the strong capillary forces between PDMS pre-polymer and PDMS submicrobeads/EGO sheets (a possible particle structure in the dispersion is shown in Fig. S5) [23]. In this nanocomposite, the PDMS submicrobeads/EGO sheets, PDMS pre-polymer and water respectively play roles as solid suspended particles, capillary bridge, and continuous medium. Ultimately, a homogenous and extrudable gel-like ink was developed.

Rheological measurements were conducted at ambient temperature on the PDMS submicrobead/EGO nanocomposite ink. As shown in Fig. 3a, the nanocomposite ink exhibit a typical shear thinning thixotropic fluid behavior; that is, the apparent viscosity decreased with increasing shear rate [41]. At a low shear rate of 0.009 s^{-1} the ink exhibited a high apparent viscosity of 1242 Pa s. As the shear rate is increased to 0.881 s^{-1}, the shear stress was 42.54 Pa (Fig. 3b), and the apparent viscosity was reduced to 48.3 Pa s (Fig. 3a). This shear thinning behavior is essential to ensure a smooth flow of ink. The ink was able to easily flow through the 3D printer's nozzles (50–200 μm) and form extruded filament with diameters ranging from 50 to 200 μm. Examples of these extruded filaments are shown in Fig. S6.

The rheological behavior of the ink was further elucidated by comparing its elastic/storage modulus (G') and viscous/loss modulus (G'') in Fig. 3c and d. At a low shear stress of 11.9 Pa, the ink exhibited higher G' of ~2500 Pa than G'' of ~550 Pa (Fig. 3c).

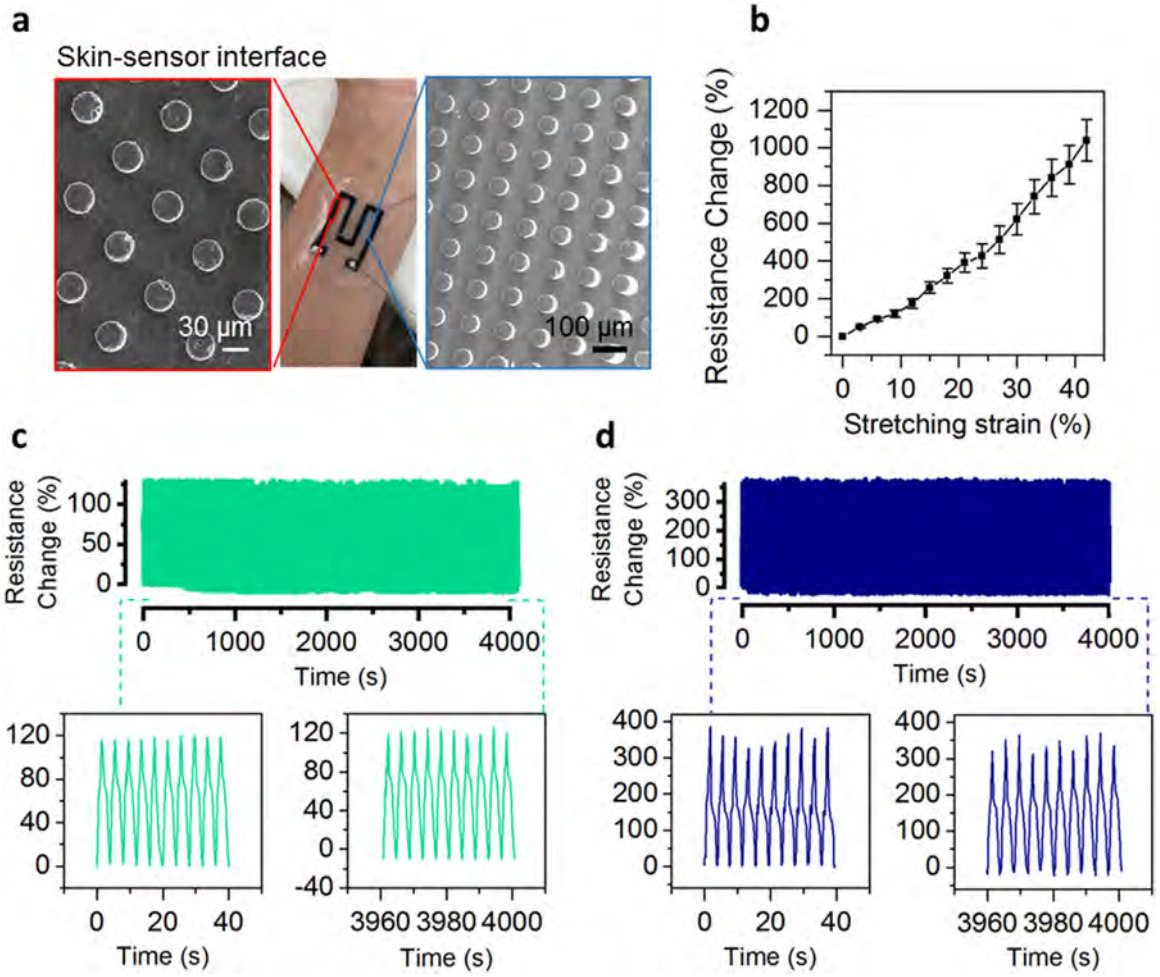

Fig. 4. Wearable, stretchable strain sensing patch images and characterization. (a) The macro-size strain sensor attached to the forearm. SEM images show the underside of the sensor where it attaches to the skin, including a segment of the patch containing the printed ink (left panel) and a section containing pure PDMS (right panel). (b) Relative resistance change of the sensor versus applied strain. (c–d) Resistance change over 1000 cycles for tensile strains of 10% (c) and 20% (d) of the original length at a frequency of 0.25 Hz (4 s/cycle); bottom panels show the enlarged view of the data in the initial and final 10 cycles. The resistance change is measured as a percentage of the resting/baseline resistance.

Correspondingly, at a low shear strain of 0.02, G' was ~3200 Pa, and G'' was 770 Pa (Fig. 3d). This elastic solid like behavior (higher storage modulus at low shear stress and low shear rate) ensures the ink is able to retain its structure after printing [21]. At a high shear stress of 49 Pa, G' drops dramatically and eventually becomes lower than G'' (Fig. 3c). The results in Fig. 3c and d indicate that the ink exhibits liquid-like behavior at high shear stress, as G' is slightly lower than G'', but returns to a solid-like material at low shear stress.

For DIW, the gel-like nanocomposite ink was loaded into a syringe (Fig. 3e) and extruded onto a substrate heated to 50 °C. During the heating, the water solvent evaporated quickly and the PDMS binder was cured. Note that the PDMS submicrobeads were key to the printability of the final ink. These fillers increase the ink's viscosity while still allowing for shear thinning behavior due to the free movement of individual beads. The beads' size allows for extrusion through very small direct writing nozzles. As a general rule, dispersed nanomaterials' largest dimension should be less than ~1/50 of the nozzle diameter to avoid clogging effects, a criterion met here [42]. Moreover, these submicrobeads can uniformly disperse in suspension for more than 1 month, which helps to ensure the ink's homogeneity throughout printing and storage. The ink has the further advantage of being water-based, containing no cytotoxic solvents, and requiring only low temperature cure.

3.4. Electrical properties and thermal response of the cured ink

Moderate thermal annealing can deoxygenate GO/EGO and enhance its electrical conductivity [29]. A relatively low temperature of 200 °C was applied to the printed features for a variable amount of time (10–70 min). During this annealing, EGO sheets were deoxygenated and increased in hydrophobicity [43]. Due to increased hydrophobic interaction [44], the EGO sheets closely wrapped PDMS submicrobeads, as shown in Fig. S7. After 60 min annealing, the volume resistivity of the PDMS submicrobead/EGO nanocomposite ink (0.83 vol.% EGO) was reduced from ~40.0 to ~1.61 kΩ·cm (Fig. 3f).

The EGO volume fraction is the major determinant of the electrical conductivity and piezoresistivity of the inks. The relationship between EGO volume fraction and nanocomposite volume resistivity (Fig. 3g) exhibited typical percolation threshold behavior. A power law (Eq. (1)) was used to fit the data [30]:

$$\sigma = \sigma_0 (V_f - V_0)^t, \tag{1}$$

where σ is the electrical conductivity of the cured inks, σ_0 is the power law constant, V_f is the EGO volume fraction, V_c is the filler critical EGO volume fraction at the percolation threshold, and t is the universal critical exponent. Based on the fitting, V_c was found to be 0.72 vol.% and t was 4.45. At 0.72 vol.%, the resistivity reduced by six orders of magnitude due to the formation of an electrically conductive network. The conductivity of composites near the percolation zone tends to exhibit higher sensitivity to applied strain [5,45], so we chose the ink composed of 0.83 vol.% EGO. This exhibited a volume resistivity of ~1.66 kΩ·cm after thermal annealing at 200 °C for 1 h in air.

The composite's relatively low percolation threshold is associated with the submicrobead-based structure. At 0.83 vol.%, EGO sheets connect with each other around PDMS submicrobeads, forming an interconnected conductive network (Fig. 3h). A control ink without pre-curing the PDMS into submicrobeads had a higher percolation threshold (1.63 vol.%; Fig. S8).

The thermal response of the ink after annealing at 200 °C for 1 h was compared with a similarly annealed EGO film using thermogravimetric analysis (TGA) (Fig. S9). The thermally annealed EGO had two temperatures where large mass loss was observed, one at 300 °C, presumably due to loss of remaining oxygen-containing groups, and a second at 600 °C, due to thermal decomposition of carbon atoms. PDMS submicrobeads were able to withstand heating to 300 °C with limited weight loss [43].

3.5. DIW fabrication and testing of wearable tactile sensors

A pressure-driven syringe-style 3D printer was used to directly write the wearable tactile sensors. The PDMS submicrobead/EGO ink was extruded onto a microporous polymer template (made using SU-8 epoxy, shown in Section 10 of the Supplementary Material). After the printed part was set and thermally annealed, PDMS pre-polymer was poured over the printed sensing component. The PDMS seeped into the micropores of the SU-8 template (in the areas not already filled with ink) and encapsulated the printed parts. After attaching electrodes and curing, this resulted in a robust silicone sensor patch with an array of micropillars on one side (Fig. 4a). The fabrication procedure is illustrated in Figs. S10 and S11. The micropillars act as a dry adhesive, allowing the sensor to durably attach onto human skin via van der Waals forces.

Under tensile loading, the sensor exhibits piezoresistivity due to the change in connectivity in the EGO network. The sensitivity of this piezoresistivity was evaluated by a gauge factor (GF), calculated as:

$$\mathrm{GF} = \frac{\Delta R/R_0}{\varepsilon}, \tag{2}$$

where ΔR is the resistance change of the sensor under strain, R_0 is the resistance prior to straining, and ε is the applied strain. Under tensile loading, EGO sheets flatten and slide across each other with deformation of the PDMS, in a mechanism similar to that previously described [15,46,47]. EGO sheets closely associate with PDMS submicrobeads as well as the PDMS binder/scaffold due to hydrophobic interactions [48]. As the PDMS is stretched, the EGO will stretch along with it. Linear changes in the scaffold lead to linear increases in ohmic resistance within a certain strain region. The sensor can therefore show an approximately linear response in resistivity up to 40% tensile strain with a gauge factor of 20.0 ± 2.8 (Fig. 4b).

The sensor also exhibits high durability, as shown in Fig. 4c and d. It responds to cyclic tensile strain with remarkable stability and reproducibility during 1000 cycles of 10% and 20% strain at a frequency of 0.25 Hz. The resistance change curves of the first and last 10 cycles are similar, confirming the consistent response to load. Furthermore, the strain sensor exhibited a rapid response (83 ms) to initial strain (Fig. S12).

The wearable sensors can be adopted for real-time monitoring of various human movements. The sensor detected strain from elbow bending (Fig. 5a) and finger touching (Fig. 5b). The sensor can also detect a minor strain from slight finger bending (Fig. 5c). Lastly, due to the dry adhesive substrate's robust, conformal contact with the skin, even slight strain from a pulse at ~1.3 beats per second can be clearly detected by the sensor (Fig. 5d). The current strain sensor performance is comparable to state-of-the-art flexible strain sensors currently reported (Table S2). Notably, in contrast to previous direct written sensors, the current sensors exhibited a linear response to large tensile strain (40%), fast responsivity (83 ms) and high sensitivity to wrist pulse. Moreover, compared with previous metal-based nanofillers such as silver, the use of relatively inexpensive and mass-producible EGO is an advantage for the application of these types of devices.

3.6. 3D DIW of multi-layered and multi-component microsensors

Many stretchable strain sensor are based on essentially planar morphologies [14,49–51] which lack sensitivity in the out-of-plane direction (i.e., the z-direction) [17,52–54]. 3D printing can introduce anisotropy in the z-direction to improve z-direction

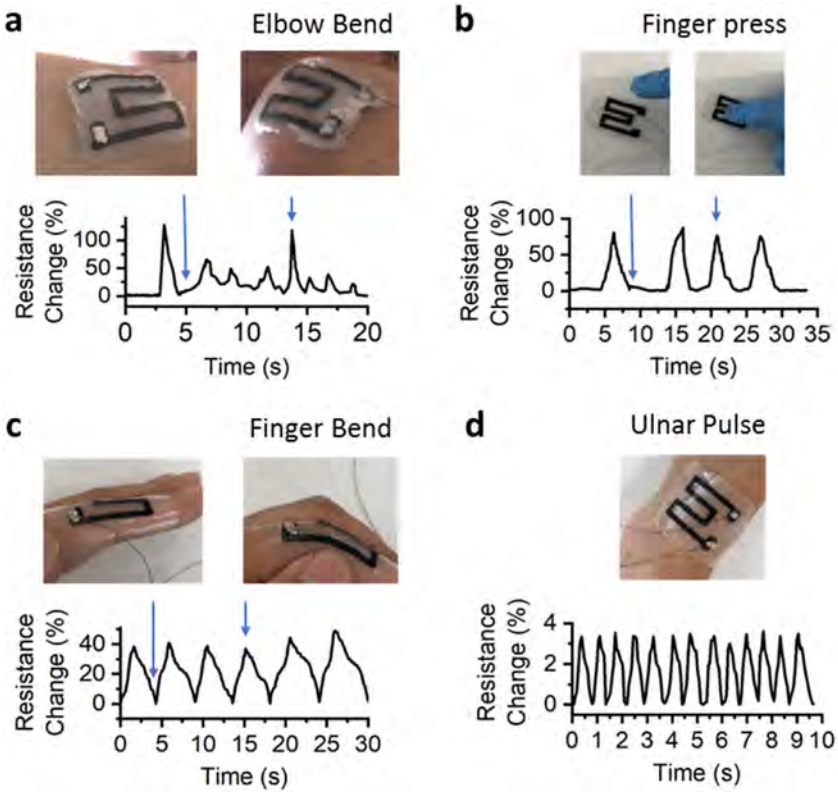

Fig. 5. Examples of applications of the wearable strain sensor. Real-time monitoring of human motion associated with (a) elbow bend, (b) finger touch, (c) finger bend and (d) ulnar arterial pulse. The resistance change is measured as a percentage of the resting/baseline resistance.

sensitivity. To compare the effect of the three-dimensional structure, three different strain sensors were 3D printed: a single-layer and triple-layer sensor composed of the nanocomposite ink only, as well as a triple-layer sensor where two layers of nanocomposite ink sandwiched an insulating layer of pure PDMS submicrobeads. For this insulating layer, a centrifuged PDMS submicrobead suspension (without the EGO or surfactant) with a concentration of 500 mg/ml was used (as described in the Experimental Section and Section 14 of the Supplementary Material). Using multi-material printing of the nanocomposite ink and PDMS submicrobeads, we integrated various functional components into the microsensors. To demonstrate the utility of the conductive ink for very high resolution DIW, the sensors were printed with a 100 μm nozzle. The top view and side view of the printed sensors are shown in Fig. 6a–f.

The pressure sensitivity of the sensors was first measured. The pressure sensitivity can be defined as [52]:

$$S = \frac{\Delta R/R_0}{\Delta P}, \tag{3}$$

where ΔR is the resistance change of the sensor under strain, R_0 is the resistance prior to straining, and ΔP is the applied pressure. The pressure sensitivity of the microsensors was measured by placing small pieces of glass (Fig. S15a) or metal weights (Fig. S15b) onto the sensor surface. As shown in Fig. 6g–i, when a pressure was applied to the top of the single-layer sensor or triple-layer sensor with PDMS insulating layer, the resistance increased. Based on the application of 1.178 kPa, sensitivities of 0.08, 0.11 and 0.31 kPa^{-1} were recorded for the single-layer, triple-layer sensor and triple-layer sensor with insulator, respectively. Notably, the triple-layer sensor without insulating layer exhibited a negative resistance change upon pressure loading. This is due to very small void spaces or "microgaps" between layers (Fig. S16). As shown in Fig. S16b, these microgaps consist of several holes several micrometer in diameter. Upon pressure loading, the microgaps between layers are closed as the adjacent layers are compressed. As the layers come into contact with each other, additional conductive pathways are formed, reducing the resistance [52]. Thus, the 3D morphology can be used to modify the mechanism of piezoresistivity.

Control of the 3D morphology can also be used to change the sensitivity of the sensor. Compared with the single-layer and triple-layer sensor, the triple-layer sensor is clearly more sensitive; for example, upon application of 248 Pa (Fig. 6g and i), the resistance immediately increased to 0.55% of baseline for the single-layer sensor, but to 2% for the triple-layer sensor with the insulating layer. To explain this effect, it may be due to the flattened first layer from the direct printing onto the heated print-bed/silicon, as evident from the SEM micrographs, while the subsequent printed layers appeared to be thicker. This interesting substrate-induced effect will require further investigation in future study.

The sensors are characterized by a very large operating range. In addition to slight pressure associated with a small glass piece (248 Pa, 20 mg) the sensors can also monitor much larger pressure loadings (at least 500 kPa, 40 g). Fig. 6j–l shows the typical resistance response curve of microsensors with progressively increasing pressure loading. Each response curve is composed of a low-pressure and high-pressure regime. At lower loadings (less than ~12.4 kPa), resistance rapidly and linearly increases. The fitted sensitivities are 0.033 kPa^{-1} (single-layer sensor), 0.088 kPa^{-1} (triple-layer sensor) and 0.134 kPa^{-1} (triple-layer sensor with insulating layer) for the low pressure region. The mechanism behind these resistance changes is likely multifaceted. At low pressures, EGO sheets deform to generate the initial resistance change, and the sheets slide past each other, following the strain. The overlap area between EGO sheets reduces, resulting in a decrease in electron carrier density. Further increase of applied pressure can deform the PDMS submicrobeads, disconnect EGO sheets, and change the

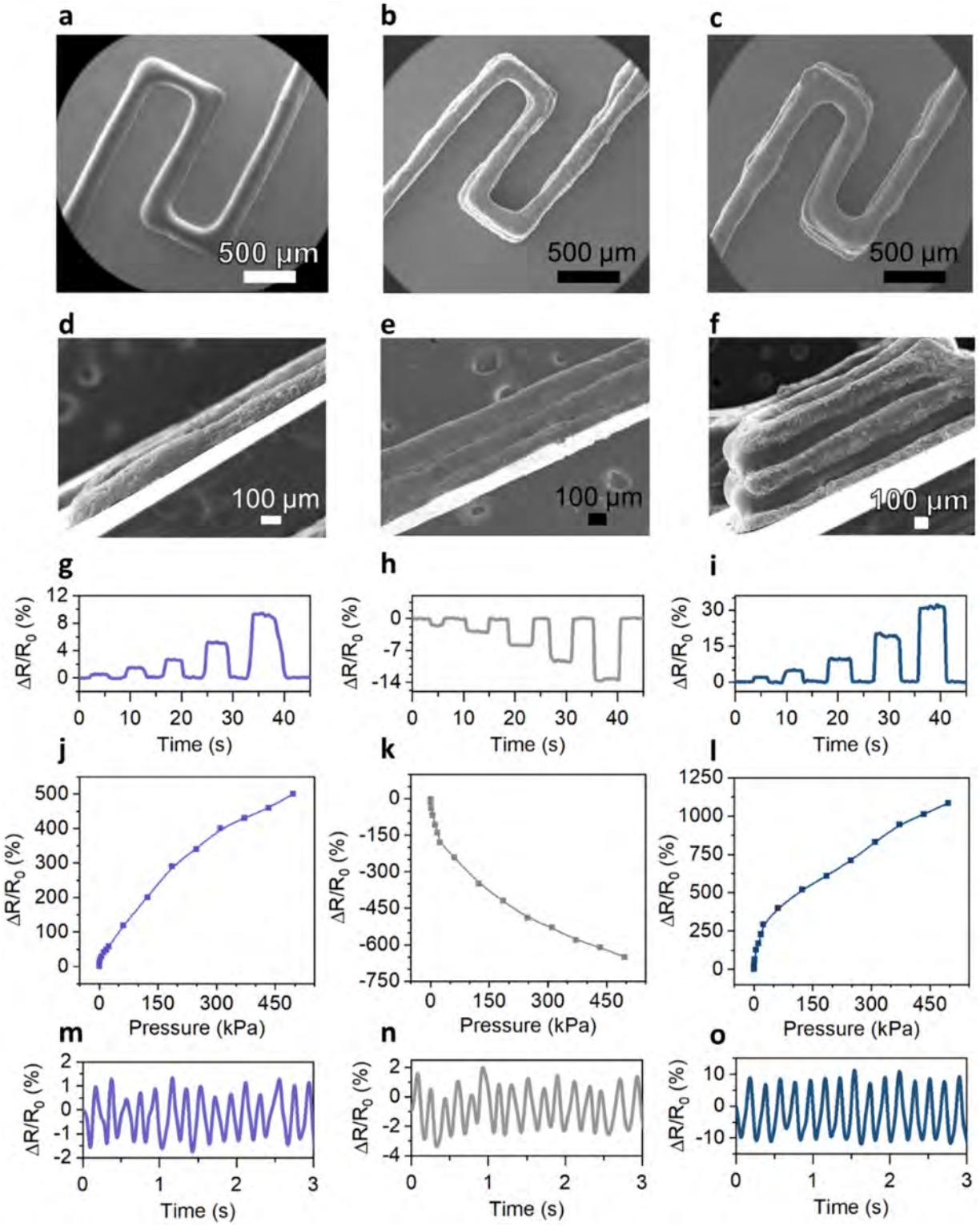

Fig. 6. SEM micrographs of top view (a, b and c) and side view (d, e and f) of the micron-scale strain sensors. (g–i) relative resistance change of the sensor ($\Delta R/R_0$) in response to 248 Pa, 372 Pa, 558 Pa, 930 Pa, and 1.178 kPa pressures applied and removed in sequence. (j–k) Resistance change of the sensors as a function of applied pressures between 0 and 500 kPa. (m–n) Resistance response to the vibrations of a vortex mixer. The first column of images/data corresponds to the single-layer sensor, the second to the triple-layer sensor without insulating layer, and the third to the triple-layer sensor with insulating layer.

morphology of small voids in the material (micro-dimples, shown in Fig. S17). As pressure transitions to the second regime, resistance increases linearly following the pressure-induced morphological changes in the bulk PDMS matrix.

To demonstrate the temporal resolution of the sensors, the microsensors were glued onto the fingertip of a glove (Fig. S18a) and used to monitor the high-frequency vibration of a vortex mixer (Fig. S18b). The recorded pressure signal (Fig. 6m–o)

had a frequency of 5 Hz, matching the set vibrations of the vortex mixer (300 rpm setting). The amplitude and waveform of the triple-layer sensor with insulator was more consistent and contained less noise than the other sensors. This stability can be attributed to the slight cushioning effect of the PDMS submicrobead layer.

These results provide two important proofs of concept. Firstly, compared with traditional fabrication technologies, 3D DIW is able to accurately control the deposition of ink and can create unique, high-resolution features such as microgaps. Secondly, with multi-material printing, we can integrate various functional components, such as the PDMS submicrobead layer, into the 3D sensor. This precise control over the structure of the sensor allows us to manipulate its function. Engineering in tiny heterojunctions between materials allows us to modulate the mechanism and magnitude of piezoresistivity.

Notably, the printed sensors are extremely thin. The single layer sensor is only ~100 μm thick, yet still has excellent sensitivity and operating range. To the best of our knowledge, this is the thinnest flexible strain sensor that has been 3D printed (Table S2, Section 13 of the Supplementary Material). This miniaturization is possible not only because of the high resolution of the printer, but equally because of the unique ink properties. The viscoelasticity imparted by the submicrobeads prevents the ink from splaying on the build platform, maintaining the printer's inherent resolution. Moreover, unlike previously reported microporous or sponge-like printed inks [11,49,55], the current PDMS is relatively dense. This compact and conductive microstructure allows the filament to be very small, yet still show high piezoresistivity.

4. Conclusion

We have developed the first 3D extrudable PDMS/graphene aqueous ink based on a PDMS submicrobeads/EGO nanocomposite, which enables high-resolution 3D DIW of strain sensors with strong performance at both large and minute length scales. To overcome the challenge of printing PDMS, rheology-tuning PDMS submicrobeads were developed. The nanocomposite ink contains PDMS submicrobeads, EGO sheets and PDMS prepolymer. Owing to the binding effect of PDMS prepolymer and agglomeration of PDMS submicrobeads/EGO, the ink possessed viscoelastic behavior, is flowable at high shear stress and possesses high storage moduli to maintain its structure after extrusion. Due to the unique viscoelastic behavior and suitable size of PDMS submicrobeads/EGO, the ink can be easily extruded through a nozzle with a diameter as small as 50 μm. We 3D printed the ink into several tactile sensing devices. A pocket-sized, flexible, stretchable, wearable strain sensing patch demonstrated high linear sensitivity (gauge factor 20.3) at a high tensile strain of 40%, short response time (83 ms) and robustness (1000 tensile cycles). Furthermore, DIW was used to produce some of the smallest and thinnest reported flexible micro-strain sensors with high resolution (100 μm), excellent sensitivity (0.3 kPa^{-1}) and large operating range (0–500 kPa). Multi-material printing was used to control the interface between printed materials at the micron-scale and to enhance the function of the sensors. The nanocomposite ink and DIW approach developed here demonstrates a practical path toward miniaturization and micro-manipulation of flexible tactile sensors. Evidently, there are many interesting materials and structural effects induced during DIW that require further study. They include the interfacial effect of the layer-by-layer structure and microgaps on the sensitivity, the effect of circuit connections between the various sensors/electrodes, the optimization of printable inks to produce unique porous structures and, in particular, the integration of other electronic components via DIW for the development of multifunctional wearable devices.

Acknowledgements

The authors acknowledge the support from the Australian Research Council (LP160101521 and DP170104157). The authors thank Dr. Dongchen Qi for his assistance in the XPS data collection.

Appendix A. Supplementary data

Supplementary data associated with this article can be found, in the online version, at doi:10.1016/j.apmt.2019.06.016.

References

[1] Y. Fu, X. Cai, H. Wu, Z. Lv, S. Hou, M. Peng, X. Yu, D. Zou, Fiber supercapacitors utilizing pen ink for flexible/wearable energy storage, Adv. Mater. 24 (2012) 5713–5718, http://dx.doi.org/10.1002/adma.201202930.
[2] C. Zhao, Y. Liu, S. Beirne, J. Razal, J. Chen, Recent development of fabricating flexible micro-supercapacitors for wearable devices, Adv. Mater. Technol. 3 (2018) 1800028, http://dx.doi.org/10.1002/admt.201800028.
[3] I. Hwang, H.N. Kim, M. Seong, S.H. Lee, M. Kang, H. Yi, W.G. Bae, M.K. Kwak, H.E. Jeong, Multifunctional smart skin adhesive patches for advanced health care, Adv. Healthcare Mater. 7 (2018) 1800275, http://dx.doi.org/10.1002/adhm.201800275.
[4] H.C. Ko, M.P. Stoykovich, J. Song, V. Malyarchuk, W.M. Choi, C.-J. Yu, J.B. Geddes Iii, J. Xiao, S. Wang, Y. Huang, A hemispherical electronic eye camera based on compressible silicon optoelectronics, Nature 454 (2008) 748–753, http://dx.doi.org/10.1038/nature07113.
[5] S.-Z. Guo, K. Qiu, F. Meng, S.H. Park, M.C. McAlpine, 3D printed stretchable tactile sensors, Adv. Mater. 29 (2017) 1701218, http://dx.doi.org/10.1002/adma.201701218.
[6] S. Gong, W. Schwalb, Y. Wang, Y. Chen, Y. Tang, J. Si, B. Shirinzadeh, W. Cheng, A wearable and highly sensitive pressure sensor with ultrathin gold nanowires, Nat. Commun. 5 (2014) 3132, http://dx.doi.org/10.1038/ncomms4132.
[7] S. Gong, D.T. Lai, B. Su, K.J. Si, Z. Ma, L.W. Yap, P. Guo, W. Cheng, Highly stretchy black gold E-skin nanopatches as highly sensitive wearable biomedical sensors, Adv. Electron. Mater. 1 (2015) 1400063, http://dx.doi.org/10.1002/aelm.201400063.
[8] S. Seyedin, P. Zhang, M. Naebe, S. Qin, J. Chen, X. Wang, J.M. Razal, Textile strain sensors: a review of the fabrication technologies, performance evaluation and applications, Mater. Horiz. 6 (2019) 203–210, http://dx.doi.org/10.1039/c8mh01062e.
[9] D. Wang, Y. Zhang, X. Lu, Z. Ma, C. Xie, Z. Zheng, Chemical formation of soft metal electrodes for flexible and wearable electronics, Chem. Soc. Rev. 47 (2018) 4611–4641, http://dx.doi.org/10.1039/c7cs00192d.
[10] T.J. Hinton, A. Hudson, K. Pusch, A. Lee, A.W. Feinberg, 3D printing PDMS elastomer in a hydrophilic support bath via freeform reversible embedding, ACS Biomater. Sci. Eng. 2 (2016) 1781–1786, http://dx.doi.org/10.1021/acsbiomaterials.6b00170.
[11] Q. Chen, J. Zhao, J. Ren, L. Rong, P.-F. Cao, R.C. Advincula, 3D printed multifunctional, hyperelastic silicone rubber foam, Adv. Funct. Mater. 29 (2019) 1900469, http://dx.doi.org/10.1002/adfm.201900469.
[12] J.T. Muth, D.M. Vogt, R.L. Truby, Y. Mengüç, D.B. Kolesky, R.J. Wood, J.A. Lewis, Embedded 3D printing of strain sensors within highly stretchable elastomers, Adv. Mater. 26 (2014) 6307–6312, http://dx.doi.org/10.1002/adma.201400334.
[13] J. Lv, Z. Gong, Z. He, J. Yang, Y. Chen, C. Tang, Y. Liu, M. Fan, W.-M. Lau, 3D printing of a mechanically durable superhydrophobic porous membrane for oil–water separation, J. Mater. Chem. A 5 (2017) 12435–12444, http://dx.doi.org/10.1039/c7ta02202f.
[14] H.-J. Kim, A. Thukral, C. Yu, Highly sensitive and very stretchable strain sensor based on a rubbery semiconductor, ACS Appl. Mater. Interfaces 10 (2018) 5000–5006, http://dx.doi.org/10.1021/acsami.7b17709.
[15] G. Shi, Z. Zhao, J.H. Pai, I. Lee, L. Zhang, C. Stevenson, K. Ishara, R. Zhang, H. Zhu, J. Ma, Highly sensitive, wearable, durable strain sensors and stretchable conductors using graphene/silicon rubber composites, Adv. Funct. Mater. 26 (2016) 7614–7625, http://dx.doi.org/10.1002/adfm.201602619.
[16] G. Shi, T. Liu, Z. Kopecki, A. Cowin, I. Lee, J.-H. Pai, S.E. Lowe, Y.L. Zhong, A multifunctional wearable device with a graphene/silver nanowire nanocomposite for highly sensitive strain sensing and drug delivery, C J. Carbon Res. 5 (2019) 17, http://dx.doi.org/10.3390/c5020017.
[17] M.D. Ho, Y. Ling, L.W. Yap, Y. Wang, D. Dong, Y. Zhao, W. Cheng, Percolating network of ultrathin gold nanowires and silver nanowires toward "invisible" wearable sensors for detecting emotional expression and apexcardiogram, Adv. Funct. Mater. 27 (2017) 1700845, http://dx.doi.org/10.1002/adfm.201700845.
[18] M. Abshirini, M. Charara, Y. Liu, M. Saha, M.C. Altan, 3D printing of highly stretchable strain sensors based on carbon nanotube nanocomposites, Adv. Eng. Mater. 20 (2018) 1800425, http://dx.doi.org/10.1002/adem.201800425.
[19] K. Fu, Y. Yao, J. Dai, L. Hu, Progress in 3D printing of carbon materials for energy-related applications, Adv. Mater. 29 (2017) 1603486, http://dx.doi.org/10.1002/adma.201603486.

[20] P. Chang, H. Mei, S. Zhou, K.G. Dassios, L. Cheng, 3D printed electrochemical energy storage devices, J. Mater. Chem. A 7 (2019) 4230, http://dx.doi.org/10.1039/c8ta11860d.
[21] Y. Liu, B. Zhang, Q. Xu, Y. Hou, S. Seyedin, S. Qin, G.G. Wallace, S. Beirne, J.M. Razal, J. Chen, Development of graphene oxide/polyaniline inks for high performance flexible microsupercapacitors via extrusion printing, Adv. Funct. Mater. 28 (2018) 1706592, http://dx.doi.org/10.1002/adfm.201706592.
[22] Y. Yang, Q. Huang, L. Niu, D. Wang, C. Yan, Y. She, Z. Zheng, Waterproof, ultrahigh areal-capacitance, wearable supercapacitor fabrics, Adv. Mater. 29 (2017) 1606679, http://dx.doi.org/10.1002/adma.201606679.
[23] S. Roh, D.P. Parekh, B. Bharti, S.D. Stoyanov, O.D. Velev, 3D printing by multiphase silicone/water capillary inks, Adv. Mater. 29 (2017) 1701554, http://dx.doi.org/10.1002/adma.201701554.
[24] H. Yang, W.R. Leow, X. Chen, 3D printing of flexible electronic devices, Small Methods 2 (2018) 1700259, http://dx.doi.org/10.1002/smtd.201700259.
[25] M. Jin, X. Feng, J. Xi, J. Zhai, K. Cho, L. Feng, L. Jiang, Super-hydrophobic PDMS surface with ultra-low adhesive force, Macromol. Rapid Commun. 26 (2005) 1805–1809, http://dx.doi.org/10.1002/marc.200500458.
[26] S. Dewasthale, C. Andrews, D. Graiver, R. Narayan, Water soluble polysiloxanes, Silicon 9 (2017) 619–628, http://dx.doi.org/10.1007/s12633-015-9334-3.
[27] L. Montazeri, S. Bonakdar, M. Taghipour, P. Renaud, H. Baharvand, Modification of PDMS to fabricate PLGA microparticles by a double emulsion method in a single microfluidic device, Lab. Chip 16 (2016) 2596–2600, http://dx.doi.org/10.1039/c6lc00437g.
[28] D.J. McClements, S.M. Jafari, Improving emulsion formation, stability and performance using mixed emulsifiers: a review, Adv. Colloid Interface Sci. 251 (2018) 55–79, http://dx.doi.org/10.1016/j.cis.2017.12.001.
[29] S.E. Lowe, G. Shi, Y. Zhang, J. Qin, S. Wang, A. Uijtendaal, J. Sun, L. Jiang, S. Jiang, D. Qi, M. Al-Mamun, P. Liu, Y.L. Zhong, H. Zhao, Scalable production of graphene oxide using a 3D-printed packed-bed electrochemical reactor with a boron-doped diamond electrode, ACS Appl. Nano Mater. 2 (2019) 867–878, http://dx.doi.org/10.1021/acsanm.8b02126.
[30] S. Chen, Y. Song, D. Ding, Z. Ling, F. Xu, Flexible and anisotropic strain sensor based on carbonized crepe paper with aligned cellulose fibers, Adv. Funct. Mater. 28 (2018) 1802547, http://dx.doi.org/10.1002/adfm.201802547.
[31] G. Shi, S. Araby, C.T. Gibson, Q. Meng, S. Zhu, J. Ma, Graphene platelets and their polymer composites: fabrication, structure, properties, and applications, Adv. Funct. Mater. 28 (2018) 1706705, http://dx.doi.org/10.1002/adfm.201706705.
[32] M. Yi, Z. Shen, A review on mechanical exfoliation for the scalable production of graphene, J. Mater. Chem. A 3 (2015) 11700–11715, http://dx.doi.org/10.1039/c5ta00252d.
[33] J. Zeng, H. Haoqing, A. Schaper, H. Wendorff Joachim, A. Greiner, Poly-L-lactide nanofibers by electrospinning – influence of solution viscosity and electrical conductivity on fiber diameter and fiber morphology, e-Polymers 3 (2003) 1, http://dx.doi.org/10.1515/epoly.2003.3.1.102.
[34] Z. Wei, J. Li, C. Wang, J. Cao, Y. Yao, H. Lu, Y. Li, X. He, Thermally stable hydrophobicity in electrospun silica/polydimethylsiloxane hybrid fibers, Appl. Surf. Sci. 392 (2017) 260–267, http://dx.doi.org/10.1016/j.apsusc.2016.09.057.
[35] M.T. Shaw, On estimating the zero-shear-rate viscosity: tests with PIB and PDMS, AIP Conf. Proc. 1779 (2016) 070011, http://dx.doi.org/10.1063/1.4965543.
[36] I. Svorstol, T. Sigvartsen, T. Songstad, L. Ernster, H. Lönnberg, J. Berg, Solvent properties of dichloromethane. VII. Viscosity studies of electrolytes in dichloromethane, Acta Chem. Scand. B. 42 (1988) 133–144.
[37] P. Yu, S.E. Lowe, G.P. Simon, Y.L. Zhong, Electrochemical exfoliation of graphite and production of functional graphene, Curr. Opin. Colloid Interface Sci. 20 (2015) 329–338, http://dx.doi.org/10.1016/j.cocis.2015.10.007.
[38] P. Yu, Z. Tian, S.E. Lowe, J. Song, Z. Ma, X. Wang, Z.J. Han, Q. Bao, G.P. Simon, D. Li, Y. Zhong, Mechanically-assisted electrochemical production of graphene oxide, Chem. Mater. 28 (2016) 8429–8438, http://dx.doi.org/10.1021/acs.chemmater.6b04415.
[39] S.E. Lowe, Y. Zhong, Challenges of industrial-scale graphene oxide production, in: A.M. Dimiev, S. Eigler (Eds.), Graphene Oxide. Fundamentals and Applications, John Wiley & Sons, Oxford, 2015.
[40] A. Manosroi, P. Wongtrakul, J. Manosroi, H. Sakai, F. Sugawara, M. Yuasa, M. Abe, Characterization of vesicles prepared with various non-ionic surfactants mixed with cholesterol, Colloids Surf. B Biointerfaces 30 (2003) 129–138, http://dx.doi.org/10.1016/S0927-7765(03)00080-8.
[41] Z. Wang, H. Gao, Q. Zhang, Y. Liu, J. Chen, Z. Guo, Recent advances in 3D graphene architectures and their composites for energy storage applications, Small 15 (2019) 1803858, http://dx.doi.org/10.1002/smll.201803858.
[42] F. Bonaccorso, A. Bartolotta, J.N. Coleman, C. Backes, 2D-crystal-based functional inks, Adv. Mater. 28 (2016) 6136–6166, http://dx.doi.org/10.1002/adma.201506410.
[43] S.-W. Ng, N. Noor, Z. Zheng, Graphene-based two-dimensional Janus materials, NPG Asia Mater. 10 (2018) 217–237, http://dx.doi.org/10.1038/s41427-018-0023-8.
[44] L. Yang, Z. Wang, Y. Ji, J. Wang, G. Xue, Highly ordered 3d graphene-based polymer composite materials fabricated by "particle-constructing" method and their outstanding conductivity, Macromolecules 47 (2014) 1749–1756, http://dx.doi.org/10.1021/ma402364r.
[45] S. Wu, R.B. Ladani, J. Zhang, K. Ghorbani, X. Zhang, A.P. Mouritz, A.J. Kinloch, C.H. Wang, Strain sensors with adjustable sensitivity by tailoring the microstructure of graphene aerogel/PDMS nanocomposites, ACS Appl. Mater. Interfaces 8 (2016) 24853–24861, http://dx.doi.org/10.1021/acsami.6b06012.
[46] C. Liao, M. Zhang, L. Niu, Z. Zheng, F. Yan, Highly selective and sensitive glucose sensors based on organic electrochemical transistors with graphene-modified gate electrodes, J. Mater. Chem. B 1 (2013) 3820–3829, http://dx.doi.org/10.1039/c3tb20451k.
[47] G. Shi, Q. Meng, Z. Zhao, H.-C. Kuan, A. Michelmore, J. Ma, Facile fabrication of graphene membranes with readily tunable structures, ACS Appl. Mater. Interfaces 7 (2015) 13745–13757, http://dx.doi.org/10.1021/am5091287.
[48] V.C. Sanchez, A. Jachak, R.H. Hurt, A.B. Kane, Biological interactions of graphene-family nanomaterials: an interdisciplinary review, Chem. Res. Toxicol. 25 (2011) 15–34, http://dx.doi.org/10.1021/tx200339h.
[49] X. Wu, Y. Han, X. Zhang, Z. Zhou, C. Lu, Large-area compliant, low-cost, and versatile pressure-sensing platform based on microcrack-designed carbon Black@ polyurethane sponge for human–machine interfacing, Adv. Funct. Mater. 26 (2016) 6246–6256, http://dx.doi.org/10.1002/adfm.201601995.
[50] A.D. Valentine, T.A. Busbee, J.W. Boley, J.R. Raney, A. Chortos, A. Kotikian, J.D. Berrigan, M.F. Durstock, J.A. Lewis, Hybrid 3D printing of soft electronics, Adv. Mater. 29 (2017) 1703817, http://dx.doi.org/10.1002/adma.201703817.
[51] L. Guan, A. Nilghaz, B. Su, L. Jiang, W. Cheng, W. Shen, Stretchable-fiber-confined wetting conductive liquids as wearable human health monitors, Adv. Funct. Mater. 26 (2016) 4511–4517, http://dx.doi.org/10.1002/adfm.201600443.
[52] Y. Lee, J. Park, S. Cho, Y.-E. Shin, H. Lee, J. Kim, J. Myoung, S. Cho, S. Kang, C. Baig, H. Ko, Flexible ferroelectric sensors with ultrahigh pressure sensitivity and linear response over exceptionally broad pressure range, ACS Nano 12 (2018) 4045–4054, http://dx.doi.org/10.1021/acsnano.8b01805.
[53] Y. Yu, Y. Zhang, K. Li, C. Yan, Z. Zheng, Bio-inspired chemical fabrication of stretchable transparent electrodes, Small 11 (2015) 3504, http://dx.doi.org/10.1002/smll.201500529.
[54] S. Yao, A. Myers, A. Malhotra, F. Lin, A. Bozkurt, J.F. Muth, Y. Zhu, A wearable hydration sensor with conformal nanowire electrodes, Adv. Healthcare Mater. 6 (2017) 1601159, http://dx.doi.org/10.1002/adhm.201601159.
[55] Z. Wang, X. Guan, H. Huang, H. Wang, W. Lin, Z. Peng, Full 3D printing of stretchable piezoresistive sensor with hierarchical porosity and multimodulus architecture, Adv. Funct. Mater. 29 (11) (2019) 1807569, http://dx.doi.org/10.1002/adfm.201807569.